


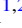




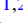

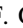


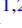




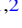
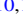
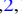







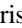
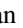
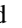





# A Warm Jupiter Transiting an M Dwarf: A TESS Single-transit Event Confirmed with the Habitable-zone Planet Finder

Caleb I. Cañas<sup>1,2,18</sup> , Gudmundur Stefansson<sup>1,2,3,18,19</sup> , Shubham Kanodia<sup>1,2</sup> , Suvrath Mahadevan<sup>1,2</sup> , William D. Cochran<sup>4</sup> , Michael Endl<sup>4</sup> , Paul Robertson<sup>5</sup> , Chad F. Bender<sup>6</sup> , Joe P. Ninan<sup>1,2</sup> , Corey Beard<sup>5</sup> , Jack Lubin<sup>5</sup> , Arvind F. Gupta<sup>1,2</sup> , Mark E. Everett<sup>7</sup> , Andrew Monson<sup>1,2</sup> , Robert F. Wilson<sup>8</sup> , Hannah M. Lewis<sup>8</sup> , Mary Brewer<sup>8</sup> , Steven R. Majewski<sup>8</sup> , Leslie Hebb<sup>9</sup> , Rebekah I. Dawson<sup>1,2</sup> , Scott A. Diddams<sup>10,11</sup> , Eric B. Ford<sup>1,2,12</sup> , Connor Fredrick<sup>10,11</sup> , Samuel Halverson<sup>13</sup> , Fred Hearty<sup>1,2</sup> , Andrea S. J. Lin<sup>1,2</sup> , Andrew J. Metcalf<sup>10,11,14</sup> , Jayadev Rajagopal<sup>7</sup> , Lawrence W. Ramsey<sup>1,2</sup> , Arpita Roy<sup>15,20</sup> , Christian Schwab<sup>16</sup> , Ryan C. Terrien<sup>17</sup> , and Jason T. Wright<sup>1,2</sup> 

<sup>1</sup> Department of Astronomy and Astrophysics, The Pennsylvania State University, 525 Davey Laboratory, University Park, PA 16802, USA; [canas@psu.edu](mailto:canas@psu.edu)

<sup>2</sup> Center for Exoplanets and Habitable Worlds, The Pennsylvania State University, 525 Davey Laboratory, University Park, PA 16802, USA

<sup>3</sup> Department of Astrophysical Sciences, Princeton University, 4 Ivy Lane, Princeton, NJ 08540, USA

<sup>4</sup> McDonald Observatory and Center for Planetary Systems Habitability, The University of Texas at Austin, Austin, TX 78730, USA

<sup>5</sup> Department of Physics and Astronomy, The University of California, Irvine, Irvine, CA 92697, USA

<sup>6</sup> Steward Observatory, The University of Arizona, 933 North Cherry Avenue, Tucson, AZ 85721, USA

<sup>7</sup> NSF's National Optical-Infrared Astronomy Research Laboratory, Tucson, AZ 85719, USA

<sup>8</sup> Department of Astronomy, University of Virginia, Charlottesville, VA 22904, USA

<sup>9</sup> Department of Physics, Hobart and William Smith Colleges, 300 Pulteney Street, Geneva, NY 14456, USA

<sup>10</sup> Time and Frequency Division, National Institute of Standards and Technology, 325 Broadway, Boulder, CO 80305, USA

<sup>11</sup> Department of Physics, University of Colorado, 2000 Colorado Avenue, Boulder, CO 80309, USA

<sup>12</sup> Institute for CyberScience, The Pennsylvania State University, University Park, PA 16802, USA

<sup>13</sup> Jet Propulsion Laboratory, California Institute of Technology, 4800 Oak Grove Drive, Pasadena, CA 91109, USA

<sup>14</sup> Space Vehicles Directorate, Air Force Research Laboratory, 3550 Aberdeen Avenue SE, Kirtland AFB, NM 87117, USA

<sup>15</sup> Department of Astronomy, California Institute of Technology, Pasadena, CA 91125, USA

<sup>16</sup> Department of Physics and Astronomy, Macquarie University, Balaclava Road, North Ryde, NSW 2109, Australia

<sup>17</sup> Department of Physics and Astronomy, Carleton College, One North College Street, Northfield, MN 55057, USA

Received 2020 May 6; revised 2020 August 3; accepted 2020 August 3; published 2020 September 2

## Abstract

We confirm the planetary nature of a warm Jupiter transiting the early M dwarf TOI-1899 using a combination of available TESS photometry; high-precision, near-infrared spectroscopy with the Habitable-zone Planet Finder; and speckle and adaptive optics imaging. The data reveal a transiting companion on an  $\sim 29$  day orbit with a mass and radius of  $0.66 \pm 0.07 M_J$  and  $1.15^{+0.04}_{-0.05} R_J$ , respectively. The star, TOI-1899, is the lowest-mass star known to host a transiting warm Jupiter, and we discuss the follow-up opportunities afforded by a warm ( $T_{\text{eq}} \sim 362$  K) gas giant orbiting an M0 star. Our observations reveal that TOI-1899.01 is a puffy warm Jupiter, and we suggest additional transit observations to both refine the orbit and constrain the true dilution observed in TESS.

*Unified Astronomy Thesaurus concepts:* [Exoplanets \(498\)](#)

## 1. Introduction

Close-orbiting Jupiter-sized exoplanets were one of the first types of exoplanets discovered. There is still no consensus as to the exact formation and migration mechanisms required to create this population. Predictions using the core accretion theory of planet formation suggest there is a low abundance of Jupiter-like planets orbiting M dwarfs (e.g., Laughlin et al. 2004). From radial velocity (RV) surveys, Jupiter-sized exoplanets are relatively rare in the Galaxy, and their occurrence rate decreases around the M dwarf population (e.g.; Endl et al. 2006; Johnson et al. 2010; Bonfils et al. 2013).

Of particular interest is the population of transiting warm Jupiters (WJs) that have periods spanning  $\sim 10$ – $200$  days because such systems allow us to probe migration pathways and test our understanding of planetary internal structures. The WJs are far enough from the host star that the stellar obliquity would remain unperturbed by tides raised on the star (Albrecht

et al. 2012; but see also Li & Winn 2016), and any inflation in their radii should occur through delayed contraction and not via stellar flux-driven or tidal mechanisms (Baraffe et al. 2014). While ground-based surveys have been important in the detection and characterization of hot Jupiters with periods  $< 10$  days, transiting WJs are challenging to discover from the ground. As of this writing, there are four known short-period ( $< 10$  days) transiting Jupiter-sized exoplanets orbiting M dwarfs: Kepler-45 b (Johnson et al. 2012), HATS-6 b (Hartman et al. 2015), NGTS-1 b (Bayliss et al. 2018), and HATS-71 b (Bakos et al. 2020). Some WJs orbiting M dwarfs have been detected through the RV method (e.g., Delfosse et al. 1998; Marcy et al. 1998; Morales et al. 2019), but none have been shown to transit.

In this paper, we confirm the planetary nature of a WJ transiting the M dwarf TOI-1899 (TIC 172370679, Gaia DR2 2073530190996615424;  $T = 12.58$ ,  $G_{RP} = 12.59$ ). We characterize the system using adaptive optics (AO) imaging with the ShaneAO instrument (Srinath et al. 2014) on the 3 m Shane Telescope at Lick Observatory, speckle imaging with the NN-EXPLORE Exoplanet Stellar Speckle Imager (NESSI; Scott et al. 2018) instrument at the WIYN 3.5 m telescope, and

<sup>18</sup> NASA Earth and Space Science Fellow.

<sup>19</sup> Henry Norris Russell Fellow.

<sup>20</sup> Robert A. Millikan Postdoctoral Fellow.

precision near-infrared (NIR) RVs obtained with the Habitable-zone Planet Finder Spectrograph (HPF; Mahadevan et al. 2012, 2014). We derive stellar parameters for TOI-1899 using our HPF spectra and use the HPF RVs to confirm the WJ nature of the transiting companion.

This paper is structured as follows. Section 2 presents the photometric and imaging observations used to analyze the false-positive probability (FPP) of this planet, and Section 3 presents the subsequent ground-based photometric and confirming spectroscopic observations of TOI-1899. Section 4 presents our best estimates of the stellar parameters, Section 5 describes the analysis of the photometry and velocimetry, Section 6 provides further discussion of the feasibility for future study of this system, and we conclude the paper in Section 7 with a summary of our key results.

## 2. Detection and Statistical Validation

### 2.1. TESS Photometry

TESS observed TIC 172370679 in Sectors 14 and 15 and has photometric data spanning 2019 July 18 through 2019 September 10. Given its single-transit nature, this target was not detected by the TESS science processing pipeline (SPOC; Jenkins et al. 2016), nor was it listed as a threshold-crossing event (TCE) by the TESS Science Office.<sup>21</sup> The TESS data validation statistics are similar to the Kepler data validation statistics, and the classification as a TCE uses the multiple event statistic (MES), a value that gives the significance of a detection when the data is folded to the calculated orbital period (Tenenbaum et al. 2013). Kepler adopted an MES threshold of  $7.1\sigma$  (Jenkins et al. 2002) to ensure there was no more than one false-alarm detection during the entirety of the Kepler mission when searching for an Earth-sized planet producing four transits around a 12th magnitude Sun-like star. Based on the data release notes for Sector 15,<sup>22</sup> TESS adopts an identical MES threshold, and any detection below this threshold, such as a single-transiting object, is rejected from further analysis. After submission of this manuscript, TIC 172370679 was identified as a community object of interest by citizen scientists in the Planet Hunters TESS project (Eisner et al. 2020) and given the designation TOI-1899.<sup>23</sup>

We identified TOI-1899.01 as a planetary candidate using a pipeline we developed to search for transiting candidates orbiting M dwarfs in the TESS short-cadence data. Our pipeline uses the `lightkurve` package (Lightkurve Collaboration et al. 2018) to detrend the data with a Savitzky–Golay filter and searches for transit events using the box least-squares algorithm (Kovács et al. 2002). This target showed a single,  $\sim 5\%$  flat-bottomed eclipsing event with a duration of  $\sim 5$  hr (Figure 1). Although only a single transit is visible in the TESS data, TOI-1899 emerged as a promising WJ candidate for further follow-up observations due to the shape of the transit and the expected large RV semi-amplitude of the planet.

We searched for additional transits in the All-Sky Automated Survey for SuperNovae (ASAS-SN; Kochanek et al. 2017) and Zwicky Transient Facility (ZTF; Masci et al. 2019). The ASAS-SN data have a mean cadence of one observation every 2 nights, but with the ASAS-SN photometric precision of

$\sim 25\%$ , only the transit of a binary star would be detected. The ZTF data have a mean cadence of one observation per night due to the simultaneous observations of the northern fields (van Roestel et al. 2019). The ZTF has a photometric precision of  $\sim 1\%$ , but published observations are too sparse to sample the transit. Together, the ASAS-SN and ZTF data span over 1500 days but reveal no additional points during the observed TESS transit or any large-amplitude photometric variations that could be attributed to a close, bound stellar companion.

For our subsequent analysis, we used the entire presearch data-conditioned time-series light curves (Ricker & Vanderpek 2018) available at the Mikulski Archive for Space Telescopes (MAST) for Sectors 14 and 15. The data were processed by the SPOC, and the resulting light curve was corrected for dilution by known contaminating sources within the photometric aperture with a dilution factor of 0.756 (CROWDSAP in the SPOC light-curve file). We assumed the transit signal was superimposed on the photometric variability and that it could be detrended using a Gaussian process. We modeled the out-of-transit flux using the `celerite` package following the procedure in Foreman-Mackey et al. (2017) in which a simple function is constructed (Equation (56) in Foreman-Mackey et al. 2017) that mimics the properties of the quasiperiodic covariance function. No additional processing was performed on the light curve.

### 2.2. Gaia Observations

Given the large pixel size of TESS, dilution and other astrophysical false-positive scenarios must be evaluated prior to validation (e.g., Sullivan et al. 2015). To investigate the impact of background stars as a source of dilution, we searched the  $11 \times 11$  TESS pixel grid centered on TOI-1899 in Gaia DR2 (Gaia Collaboration et al. 2018). We use the Gaia  $G_{RP}$  bandpass as an approximation to the TESS bandpass. Figure 2(a) presents a ZTF  $zr$  image overlaid with the TESS Sector 15 pixel grid and all stars identified in Gaia DR2 that have  $|\Delta G_{RP}| < 4$  when compared to TOI-1899.

Gaia DR2 detects a total of 36 additional stars within the TESS aperture. The brightest stellar neighbor within this aperture, TIC 172370652 (Gaia DR2 2073530190996611200;  $T = 14.42$ ,  $G_{RP} = 14.38$ ), is  $17''$  away from TOI-1899 and represents a flux ratio of  $\sim 0.19$ . Gaia DR2 reveals that TIC 172370652 is a giant star at a distance of  $2500 \pm 160$  pc and a radius of  $\sim 4.5 R_{\odot}$ . Given this size, if TIC 172370652 were the host star, the system would be an eclipsing binary.

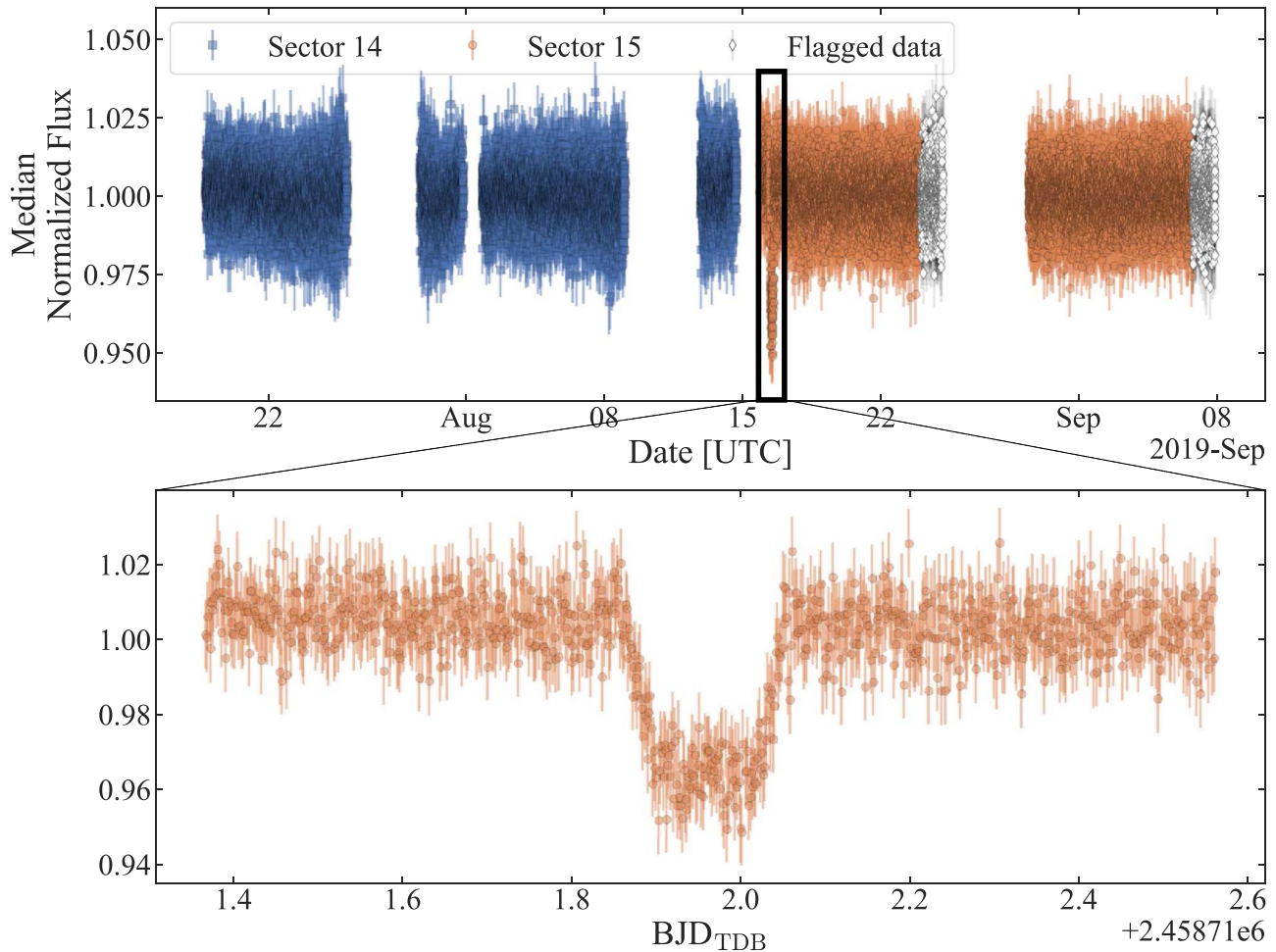
### 2.3. Centroid and Aperture Analysis

To verify further that TIC 172370652 was only a source of dilution and not the source of the eclipsing event, we analyzed both the centroids and the aperture. We calculated the centroid during the TESS transit using Discovery and Vetting of Exoplanets (DAVE; Kostov et al. 2019) to help distinguish between an eclipse occurring in the target system or in an unresolved background source. A significant centroid shift away from the purported target star during a transit is indicative of a false positive. DAVE is based on the methodology presented in Bryson et al. (2013) to compute the centroids by fitting a pixel response function model to the out-of-transit and difference images. The difference image is the difference between (i) the average of the flux before and after the transit and (ii) the flux during transit such that, in the difference image,

<sup>21</sup> [https://archive.stsci.edu/tess/bulk\\_downloads/bulk\\_downloads\\_tce.html](https://archive.stsci.edu/tess/bulk_downloads/bulk_downloads_tce.html)

<sup>22</sup> [https://archive.stsci.edu/missions/tess/doc/tess\\_dm/tess\\_sector\\_15\\_dm21\\_v02.pdf](https://archive.stsci.edu/missions/tess/doc/tess_dm/tess_sector_15_dm21_v02.pdf)

<sup>23</sup> <http://www.planethunters.org/>



**Figure 1.** TESS photometry of TOI-1899. Top: entire short-cadence PDCSAP TESS light curve for TOI-1899. Each sector is plotted with a different symbol and has been normalized by its respective median value. The white diamonds represent the data that were flagged by the TESS pipeline due to scattered-light contamination. The rectangle marks a region spanning  $\sim 1.2$  days around the single-transit event observed in Sector 15. We use all of the TESS data that are not excluded by the quality flags for analysis in this work. Bottom: enlarged version of the data contained in the rectangle. The observed transit is a single,  $\sim 5\%$  flat-bottomed event with a duration of  $\sim 5$  hr.

the pixels containing the transit are regions of excess flux. The centroids are shown in Figure 2(b). Both the out-of-transit and in-transit centroids are located in the aperture pixel containing the most flux and are separated by 0.004 pixels ( $\sim 0''.08$ ). This offset is more than 100 times smaller than the width of the point-spread function. The lack of a significant shift away from TOI-1899 during transit is consistent with this star being the host star.

We employed *eleanor* (Feinstein et al. 2019) to probe which aperture is preferred in the TESS full-frame images. We used a segment of  $31 \times 31$  pixels in the calibrated full-frame images centered on TOI-1899 to model the background and correct for systematics. Here *eleanor* derives light curves for various combinations of apertures and adopts the aperture that minimizes the combined differential photometric precision (CDPP) on the data when binned into 1 hr timescales. The CDPP was originally defined for Kepler and is formally the rms of the photometric noise on transit timescales (Jenkins et al. 2010). Minimizing this metric ensures that sharp features on relatively short timescales, such as transits, are preserved.

The preferred *eleanor* aperture is an L-shaped wedge centered on our star. Figure 2(b) presents the preferred *eleanor* aperture, which still includes the pixel containing the giant star TIC 172370652. A light curve derived with this

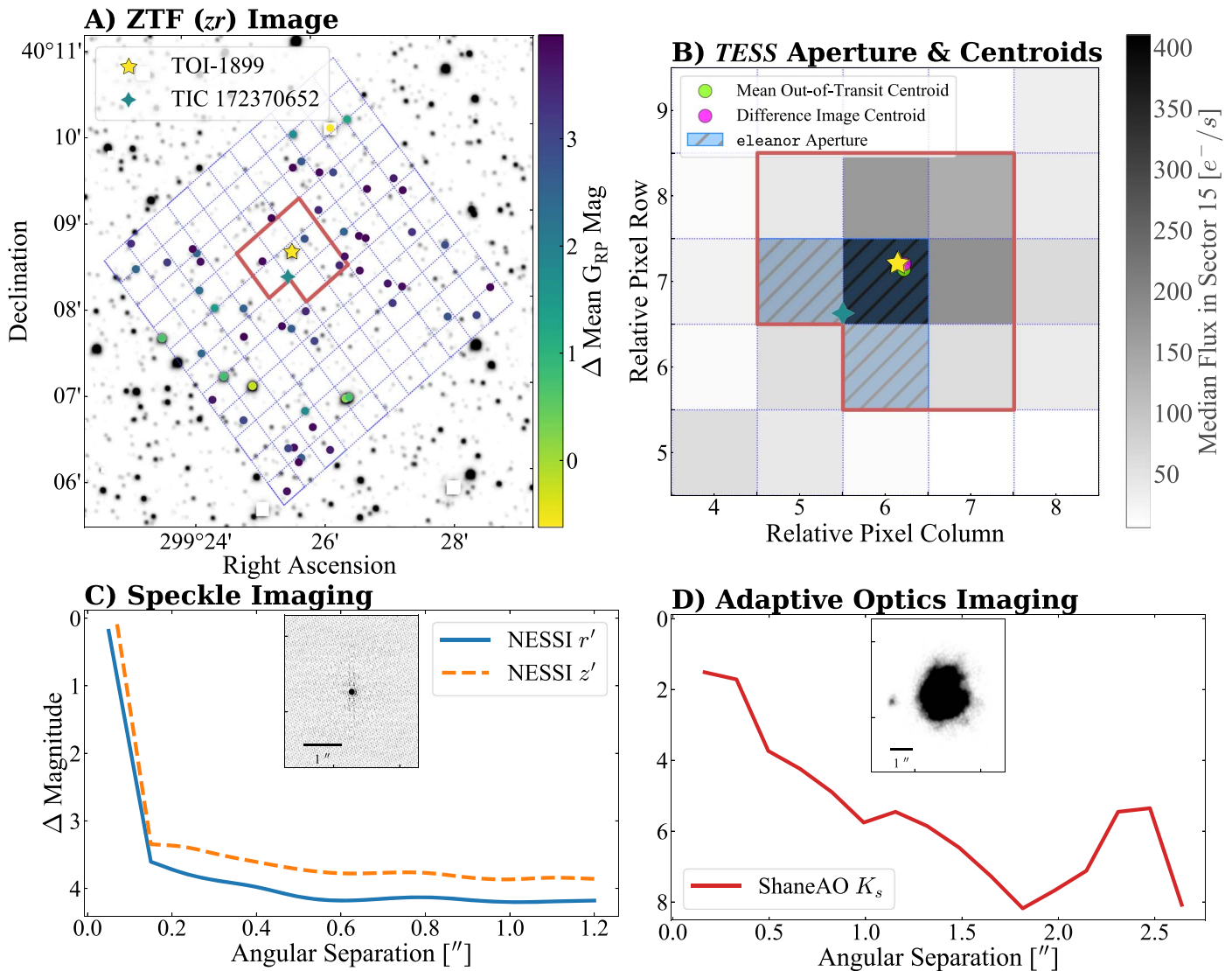
aperture from the full-frame images (using *psf\_flux* from *eleanor*) reveals a transit of identical depth to the dilution-corrected PDCSAP transit from the SPOC. Given the single-transiting nature of this object and the consistent depth, we opted to use the TESS short-cadence data for further analysis.

#### 2.4. Speckle Imaging

To probe for binary companions or background objects, we performed speckle imaging using NESSI on the 3.5 m WIYN Telescope at KPNO on 2019 November 14. Due to the faintness of TOI-1899, the images were acquired in Sloan  $r'$  and  $z'$  instead of the narrower filters that NESSI traditionally uses. The images were reconstructed following the procedures outlined in Howell et al. (2011). The NESSI contrast curves in both filters are shown in Figure 2(c), along with an inset of the  $z'$  image. The NESSI data show no evidence of blending from a bright companion at separations of  $0''.1-1''.2$ .

#### 2.5. AO Imaging

We performed high-contrast AO imaging of TOI-1899 using the 3 m Shane Telescope at Lick Observatory on 2019 November 10. The AO imaging was carried out using the upgraded SHARCS camera (Srinath et al. 2014) in the  $K_s$



**Figure 2.** Stellar neighborhood around TOI-1899. Panel (a) shows the overlay of the TESS Sector 15 footprint on a ZTF  $zr$  image and highlights TOI-1899 (star), the giant neighbor TIC 172370652 (diamond), and all stars with  $\Delta G_{RP} < 4$  (circles). The TESS aperture is outlined in bold and contains three other stars with  $\Delta G_{RP} < 4$ , causing dilution of the transit. Panel (b) displays the region around the TESS aperture. Each pixel is colored to the median flux from Sector 15. The centroid does not significantly shift away from TOI-1899 during transit, and this suggests that it is the host star. The hatched pixels denote the best aperture as determined from the full-frame images using `eleanor`. A light curve extracted with this aperture yields a transit depth identical to the short-cadence TESS data. We include the position of TOI-1899 and TIC 172370652 for reference. Panel (c) displays the  $5\sigma$  contrast curve observed from NESSI in the Sloan  $r'$  and  $z'$  filters showing no bright companions within  $1''/2$  from the host star. The  $z'$  image is shown as an inset. The horizontal line indicates the scale of  $1''$ . Panel (d) presents the  $5\sigma$  contrast curve observed from ShaneAO in the  $K_s$  filter with the detection of a  $\Delta K_s \approx 5.5$  mag companion within  $2''/4$ . The inset is the image from ShaneAO, and the horizontal line indicates the scale of  $1''$ .

bandpass. We observed TOI-1899 using a five-point dither pattern (see, e.g., Furlan et al. 2017), imaging the star at the center of the detector and in each quadrant. We took images at four positions instead of the normal five because the limitations of the telescope motors prevented us from offsetting to one of the four standard off-center dither positions. Our experience is that sufficient sky subtraction can be performed with three or more of the five standard positions without a meaningful impact on the results.

Standard image processing, including flat-fielding, sky subtraction, and subpixel image alignment, was performed with custom Python software. We computed the variance in flux in a series of concentric annuli centered on the target star in the combined image. The resulting  $5\sigma$  contrast curve is shown in Figure 2(b). From the images, we see that a faint ( $\Delta K_s \approx 5.5$ ) secondary companion is detectable at  $\sim 2''/2$ .

The amount of dilution attributable to this companion (Gaia DR2 2073530190984193280, TIC 1879763195;  $T = 18.63$ ) is negligible. These data show that there is no evidence of blending from a bright companion with up to  $2''/5$  separation.

## 2.6. Statistical Validation

We employed `VESPA` (Morton 2012) to conduct a false-positive analysis of TOI-1899.01. The algorithm validates a planet statistically by simulating and determining the likelihood of a range of astrophysical false-positive scenarios that include background eclipsing binaries (BEBs), eclipsing binaries, and hierarchical eclipsing binaries. The code generates a population for each false-positive scenario to calculate the likelihoods.

For our analysis, we set Gaussian priors on the (i) Two Micron All Sky Survey (2MASS)  $JHK$  magnitudes (Skrutskie

et al. 2006), (ii) Sloan Digital Sky Survey (SDSS)  $g'r'$  magnitudes from the AAVSO Photometric All-Sky Survey (APASS; Henden et al. 2015), (iii) Gaia DR2 parallax, and (iv) host star surface gravity, temperature, and metallicity from the TESS Input Catalog (TIC; Stassun et al. 2019), as well as a uniform prior on the visual extinction where the upper limit is determined using estimates of Galactic dust extinction by Green et al. (2019). We set the maximum radius permissible for a BEB as the radius of the TESS aperture ( $48''$ ). We constrain the maximum depth of the secondary transit as the rms of the light curve after excising the transit ( $<7700$  ppm). We include the ShaneAO and NESSI contrast curves shown in Figure 2 as additional constraints applied to the BEB population during the *vespa* analysis. For this analysis, we adopted the period of  $P = 30$  days, which we estimated by fitting the transit with a prior on the stellar density and assuming TOI-1899.01 was on a circular orbit ( $e = 0$ ).

The WJ TOI-1899.01 has an FPP of 0.004. We note that *vespa* is a tool designed for the Kepler mission that had pixels of  $\sim 4''$  in size. With the  $\sim 21''$  pixels of TESS, there will be blended stars in a given pixel. As such, we expect the FPP to be slightly underestimated for TESS photometry, particularly in crowded fields with known blends. For TOI-1899.01, our analysis reveals a marginally validated planet when adopting the threshold of FPP  $< 1\%$  used in Morton et al. (2016). The FPP was small enough to warrant subsequent spectroscopic observations.

### 3. Confirmation and Additional Observations

#### 3.1. High-resolution Doppler Spectroscopy

We obtained 15 visits of TOI-1899 using the HPF, a high-resolution ( $R \sim 55,000$ ), NIR (8080–12780 Å) spectrograph located at the 10 m Hobby–Eberly Telescope (HET) in Texas (Mahadevan et al. 2012, 2014). The HET is a fully queue-scheduled telescope with all observations executed in a queue by the HET resident astronomers (Shetrone et al. 2007). The HPF is actively temperature-stabilized and achieves  $\sim 1$  mK temperature stability long-term (Stefansson et al. 2016). We use the algorithms in the tool `HxRGPROC` for bias noise removal, nonlinearity correction, cosmic-ray correction, and slope/flux and variance image calculation (Ninan et al. 2018) of the raw HPF data. We obtained two 945 s exposures per visit, except on the first visit, where we obtained only one exposure due to poor weather. This resulted in 29 spectra with a median signal-to-noise ratio (S/N) of 65 at 1000 nm. While HPF has an NIR laser-frequency comb (LFC) calibrator that is shown to enable  $\sim 20$  cm s $^{-1}$  calibration precision and 1.53 m s $^{-1}$  RV precision on-sky (Metcalf et al. 2019), we did not use the simultaneous LFC reference calibrator to minimize the impact of scattered LFC light in the target spectrum. We performed drift correction by extrapolating the wavelength solution from other LFC exposures from the night of the observations, as discussed in Stefansson et al. (2020). This methodology enables precise wavelength calibration and drift correction up to  $\sim 30$  cm s $^{-1}$  per observation, a value much smaller than our estimated per-observation RV uncertainty for TOI-1899 (at the  $\sim 15$  m s $^{-1}$  level).

The RVs are derived following the methodology described in Stefansson et al. (2020) using a modified version of the `SpEctrum Radial Velocity AnaLyser` pipeline

(SERVAL; Zechmeister et al. 2018). SERVAL employs the template-matching technique to derive RVs (e.g., Anglada-Escudé & Butler 2012) by creating a master template from the observations to determine the Doppler shift for each individual spectrum by minimizing the  $\chi^2$  statistic. We generated the master template using all observed spectra while ignoring any telluric regions identified using a synthetic telluric-line mask generated from `telfit` (Gullikson et al. 2014), a Python wrapper to the Line-by-Line Radiative Transfer Model package (Clough et al. 2005). We calculated the barycentric correction for each epoch using `barycorrpy`, the Python implementation (Kanodia & Wright 2018) of the algorithms from Wright & Eastman (2014). The observations are plotted in the top panel of Figure 3. Table 1 presents the derived RVs, the  $1\sigma$  uncertainties, and the S/N per pixel at 1000 nm for each epoch.

#### 3.2. Ground-based Photometry

##### 3.2.1. HDI

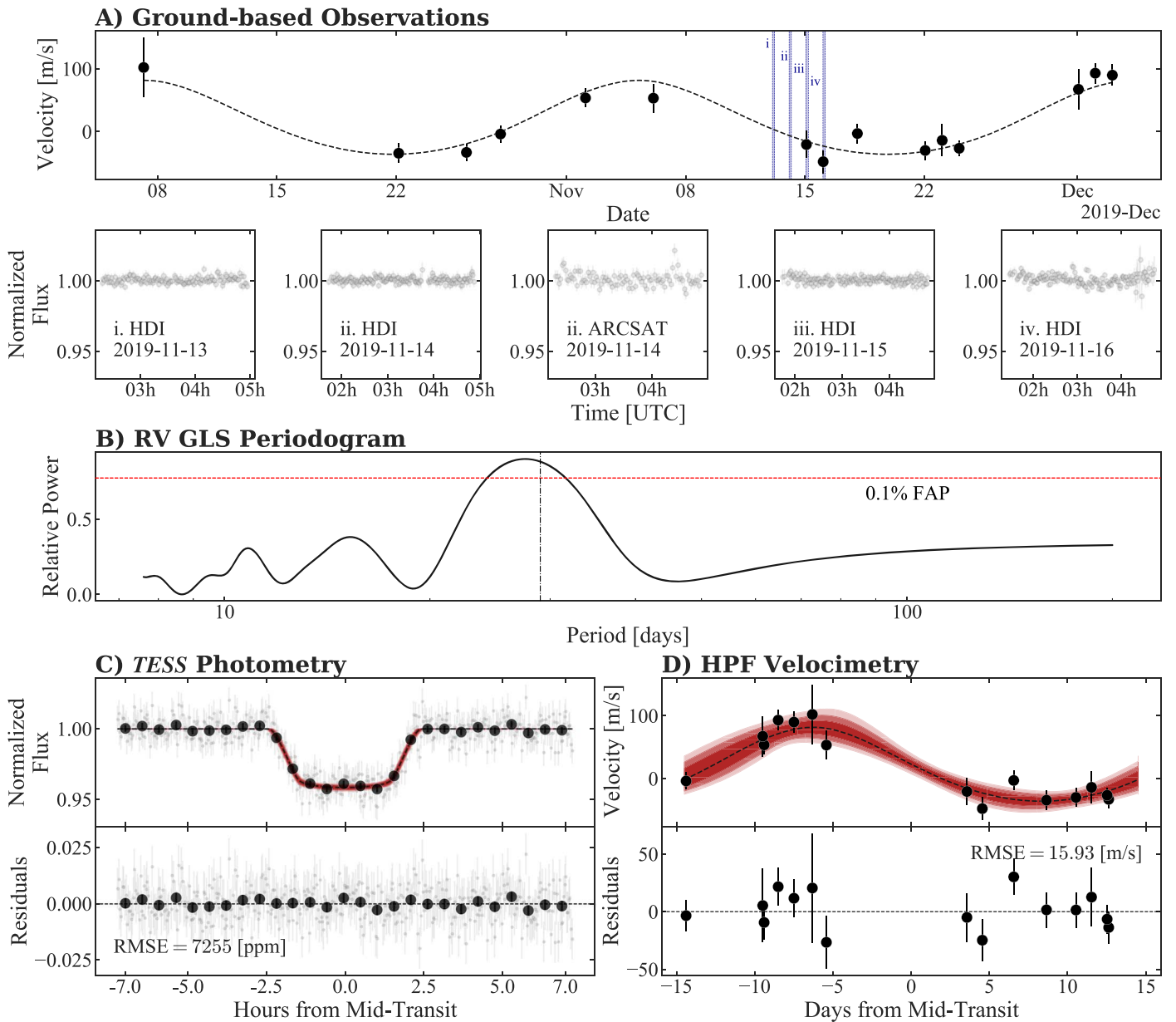
Once we obtained the first six RV measurements, it was clear that the data spanned one orbit of this system. We used a circular fit to the available HPF data to find the most probable transit times. To search for an additional transit, we observed TOI-1899 each night between 2019 November 12 and 15 with the Half-Degree Imager (HDI; Deliyannis 2013) on the WIYN 0.9 m Telescope at KPNO. The HDI has a  $4096 \times 4096$  pixel back-illuminated CCD with a  $29'2 \times 29'2$  field of view (FOV) at a plate scale of  $0''.425$  pixel $^{-1}$ . All of the observations were performed slightly defocused and in the SDSS  $z'$  filter using the  $1 \times 1$  binning mode and the four-amplifier readout mode.

We reduced the HDI observations using `AstroImageJ` (Collins et al. 2017), following the methodology described in Stefansson et al. (2017, 2018). For each night, we varied the radii of the software aperture and inner and outer background annuli in the reduction and adopted an object aperture radius of 10 pixels ( $4''.25$ ) and inner and outer sky annuli of 15 ( $6''.38$ ) and 25 ( $8''.50$ ) pixels, respectively. This configuration resulted in the minimum scatter in the photometry. Figure 2(a) presents the reduced HDI photometry, which shows no additional transits of TOI-1899.01. Subsequent observations with HPF better constrained the orbit of TOI-1899 and clarified that our ground-based observations did not coincide with the expected mid-transit time.

##### 3.2.2. ARCSAT

We observed TOI-1899 on the night of 2019 November 13 using the SDSS  $i'$  filter using FlareCam on the Astrophysical Research Consortium Small Aperture Telescope (ARCSAT) located at Apache Point Observatory. ARCSAT, formerly known as the SDSS Photometric Telescope, is a 0.5 m telescope originally used to calibrate photometry for SDSS (York et al. 2000; Tucker et al. 2006). FlareCam is optimized for fast readout times and equipped with a  $1024 \times 1024$  back-illuminated CCD for enhanced sensitivity in the blue and near-UV with an  $11'2 \times 11'2$  FOV resulting in a pixel scale of  $0''.656$  pixel $^{-1}$  (Hilton et al. 2011).

The ARCSAT observations were carried out defocused with  $2 \times 2$  binning, resulting in a pixel scale of  $1''.312$  pixel $^{-1}$ . The data were bias- and dark-subtracted and flat-field corrected with use of the Python package `ccdproc` (Craig et al. 2017). We performed aperture photometry using the Python package



**Figure 3.** Velocimetry and photometry of TOI-1899. Panel (a) presents the RVs from Table 1 along with our best-fitting model, denoted with a dashed line. The shaded regions mark the nights we obtained ground-based photometry. The second row shows the corresponding photometry from the respective instruments. For ease of comparison, the photometric vertical scales are identical to that of panel (b). No additional transits were detected on these nights. Panel (b) presents the RVs GLS periodogram of the RVs. The period from our joint fit is indicated by the vertical line. The FAP of 0.1% is shown with the horizontal line. Panel (c) presents the TESS photometry around the single-transit event, and panel (d) contains the phase-folded HPF RVs. In each case, the best-fitting model is plotted as a dashed line, while the shaded regions denote the  $1\sigma$  (darkest),  $2\sigma$ , and  $3\sigma$  range of the derived posterior solution.

Photutils (Bradley et al. 2019). We used an aperture radius of 5 pixels ( $6''5$ ) and sky subtracted with an annulus having inner and outer radii of 7 ( $9''1$ ) and 11 ( $14''3$ ) pixels, respectively. This configuration minimized the scatter in the data while avoiding flux contamination from nearby sources in the chosen apertures. The ARCSAT data in Figure 3(a) are consistent with the HDI data and show no additional transit.

## 4. Stellar Parameters

### 4.1. Spectroscopic Parameters

We employed a modified version of the `SpecMatch-Emp` algorithm (Yee et al. 2017) to characterize the properties of TOI-1899 by comparing its highest-S/N spectrum to a library

of high-resolution ( $R \sim 55,000$ ), high-quality ( $S/N > 100$ ) HPF stellar spectra that have well-determined properties from Yee et al. (2017). The modified HPF `SpecMatch-Emp` algorithm is described in Stefansson et al. (2020).

In brief, `SpecMatch-Emp` shifts the observed spectrum to the library wavelength scale, finds the best-matching library spectrum using  $\chi^2$  minimization, and uses a linear combination of the five best-matching spectra to synthesize a composite spectrum. We perform a cross-validation procedure where a spectrum from the library is removed, and we compare the recovered best-fit stellar parameter to its known library value. We repeat this comparison for the entire stellar library and adopt the standard deviation ( $\sigma$ ) of the residuals between the recovered best-fit stellar parameters and the known library

**Table 1**  
RVs of TOI-1899

BJD <sub>TDB</sub>	RV (m s <sup>-1</sup> )	$\sigma$ (m s <sup>-1</sup> )	S/N @ 1000 nm
2,458,763.683421 <sup>a</sup>	101.98	47.26	34
2,458,778.653989	-34.49	15.39	68
2,458,782.630853	-33.12	13.70	75
2,458,784.631621	-3.94	13.41	77
2,458,789.621115	53.50	14.82	71
2,458,793.603541	53.17	23.05	47
2,458,802.589058	-20.61	21.27	50
2,458,803.572612	-47.90	18.16	59
2,458,805.580779	-3.08	15.69	67
2,458,809.561619	-30.07	15.19	68
2,458,810.557411	-14.02	25.59	42
2,458,811.554959	-26.59	12.43	83
2,458,818.555145	67.27	32.03	36
2,458,819.542258	92.90	16.34	67
2,458,820.547178	89.73	16.54	64

**Notes.** All observations have exposure times of 1890 s unless otherwise indicated.

<sup>a</sup> Exposure time is 945 s.

value as the uncertainty in each measurement ( $\sigma_{T_{\text{eff}}}$ ,  $\sigma_{\text{Fe}/\text{H}}$ , and  $\sigma_{\log g}$ ).

As of this writing, the HPF *SpecMatch-Emp* library consists of 55 stars spanning the following parameter ranges:  $3100 \text{ K} < T_e < 5000 \text{ K}$ ,  $4.45 < \log g < 5.12$ , and  $-0.5 < [\text{Fe}/\text{H}] < 0.5$ . Our comparisons use the wavelength region between 10460 and 10570 Å because it is a region with minimal telluric contamination in the Y band. The derived parameters for TOI-1899 are  $T_{\text{eff}} = 3925 \pm 77 \text{ K}$ ,  $[\text{Fe}/\text{H}] = 0.20 \pm 0.13$ , and  $\log(g) = 4.68 \pm 0.05$ . These values are comparable to the photometric parameters derived with *StarHorse* (Santiago et al. 2016; Queiroz et al. 2018), a tool designed for Bayesian inference of stellar parameters and distances using data from spectroscopic surveys. The *StarHorse* values are  $T_{\text{eff}} = 3945_{-37}^{+108} \text{ K}$ ,  $\text{Fe}/\text{H} = 0.19_{-0.17}^{+0.08}$ , and  $\log(g) = 4.65 \pm 0.01$ . We adopt our *SpecMatch-Emp* parameters, as they are derived from spectra that also provide a reliable constraint on stellar metallicity. The derived spectroscopic parameters with their uncertainties are listed in Table 2. Using our HPF spectra, we also place a formal constraint of  $v \sin i_* < 2 \text{ km s}^{-1}$ .

#### 4.2. Spectral Classification

The best-matching library spectrum across all HPF spectral orders analyzed is GJ 1172, an M0 star (Gaidos et al. 2014). To confirm this spectral subtype, we used the catalog of M-type stars identified by the Large Sky Area Multi-Object Fibre Spectroscopic Telescope (LAMOST) collaboration (Zhong et al. 2019). LAMOST is a 4 m telescope equipped with 4000 fibers distributed over a 5° FOV that is capable of acquiring spectra in the optical band (3700–9000 Å) at a resolution  $R \approx 1800$  with a limiting magnitude of SDSS  $r' = 19 \text{ mag}$  (Cui et al. 2012).

The LAMOST stellar classification pipeline uses stellar templates to identify molecular absorption features (e.g., CaH, TiO) that are typical for M-type stars. To be classified as M dwarfs, targets must have (i) a mean S/N > 5 and (ii) a best-matching template that is an M type, and (iii) the spectral

indices of the absorption features must be located in the M-type stellar regime identified in Zhong et al. (2019;  $0 < \text{TiO5} < 1.2$  and  $0.6 < \text{CaH2} + \text{CaH3} < 2.4$ ).

While the metallicities of the M dwarfs are not provided, the LAMOST M dwarf catalog does include a coarse indicator of metallicity,  $\zeta$ . The value of this parameter is based on the strength of the TiO5, CaH2, and CaH3 molecular bands and quantifies the weakening of the TiO band strength due to metallicity effects (Lépine et al. 2007). Mann et al. (2013) tested the  $\zeta$  parameter with their sample and found that it correlates with  $[\text{Fe}/\text{H}]$  for supersolar metallicities but does not necessarily correlate in metal-poor M dwarfs.

The proximity of TOI-1899 to the original Kepler field resulted in two observations with LAMOST as part of their Kepler survey (Zong et al. 2018). From each observation, the spectral indices are consistent with an M0 classification. The mean value of  $\zeta = 1.326 \pm 0.003$  suggests that this is a metal-rich M dwarf. The LAMOST classification as a metal-rich M0 dwarf is in agreement with our classification from *SpecMatch-Emp*.

#### 4.3. Model-dependent Stellar Parameters

We used the EXOFASTv2 analysis package (Eastman et al. 2019) to model the spectral energy distribution (SED) and derive the stellar parameters using MIST stellar models (Choi et al. 2016; Dotter 2016). We assumed Gaussian priors using the (i) 2MASS *JHK* magnitudes; (ii) SDSS  $g'i'$  and Johnson *B* magnitudes from APASS; (iii) Wide-field Infrared Survey Explorer magnitudes (Wright et al. 2010); (iv) host star surface gravity, temperature, and metallicity derived with *SpecMatch-Emp*; and (v) distance estimate from Bailer-Jones et al. (2018). We adopt a uniform prior for the visual extinction where the upper limit is determined from estimates of Galactic dust by Green et al. (2019; Bayestar19) calculated at the distance determined by Bailer-Jones et al. (2018). We adopt the  $R_v = 3.1$  reddening law from Fitzpatrick (1999) to convert the Bayestar19 extinction to a visual magnitude extinction. The stellar priors and derived stellar parameters with their uncertainties are listed in Table 2.

### 5. Data Analysis

We employ the *juliet* analysis package (Espinoza et al. 2019) to jointly model the photometry and velocimetry. The *juliet* package utilizes publicly available tools to model the photometry (*batman*; Kreidberg 2015) and velocimetry (*radvel*; Fulton et al. 2018) and performs the parameter estimation using the importance nest-sampling algorithm *MultiNest* (Feroz et al. 2019; Buchner et al. 2014). The photometric model is based on the analytical formalism of Mandel & Agol (2002) for a planetary transit and assumes a quadratic limb-darkening law in which the limb-darkening parameters are sampled using the  $q_1$  and  $q_2$  parameterization from Kipping et al. (2013). We used the PDCSAP flux, which already corrects for dilution, so our photometric model does not include any additional dilution factor. We also set a prior on the stellar density using the value determined from our EXOFASTv2 SED fit. The RV model is a standard Keplerian model. Both the photometric and RV models include a simple white-noise model in the form of a jitter term that is added in quadrature to the error bars of each data set.

**Table 2**  
Summary of Stellar Parameters

Parameter	Description	Value	Reference
<b>Main Identifiers</b>			
TIC	...	172370679	Stassun
2MASS	...	19574239+4008357	2MASS
Gaia DR2	...	2073530190996615424	Gaia
<b>Equatorial Coordinates, Proper Motion, and Spectral Type</b>			
$\alpha_{J2000}$	Right ascension (R.A.)	19:57:42.44	Gaia
$\delta_{J2000}$	Declination (decl.)	40:08:36.05	Gaia
$\mu_\alpha$	Proper motion (R.A., mas yr <sup>-1</sup> )	35.427 ± 0.025	Gaia
$\mu_\delta$	Proper motion (decl., mas yr <sup>-1</sup> )	18.828 ± 0.029	Gaia
$D$	Dilution factor of TESS photometry	0.757	SPOC
$d$	Distance in pc	128.4 ± 0.3	Bailer-Jones
$A_{V,max}$	Maximum visual extinction	0.02	Green
Spectral type	...	M0	LAMOST
<b>Optical and NIR Magnitudes</b>			
$B$	Johnson $B$ mag	15.898 ± 0.029	APASS
$g'$	Sloan $g'$ mag	15.115 ± 0.054	APASS
$r'$	Sloan $r'$ mag	13.728 ± 0.040	APASS
$T$	TESS magnitude	12.582 ± 0.007	Stassun
$J$	$J$ mag	11.342 ± 0.022	2MASS
$H$	$H$ mag	10.666 ± 0.022	2MASS
$K_s$	$K_s$ mag	10.509 ± 0.018	2MASS
$W1$	WISE1 mag	10.412 ± 0.022	WISE
$W2$	WISE2 mag	10.460 ± 0.021	WISE
$W3$	WISE3 mag	10.312 ± 0.045	WISE
<b>Spectroscopic Parameters<sup>a</sup></b>			
$T_e$	Effective temperature in K	3925 ± 77	This work
[Fe/H]	Metallicity in dex	0.20 ± 0.13	This work
log( $g$ )	Surface gravity in cgs units	4.68 ± 0.05	This work
<b>Model-dependent Stellar SED and Isochrone Fit Parameters<sup>b</sup></b>			
$T_e$	Effective temperature in K	3841 <sup>+54</sup> <sub>-45</sub>	This work
[Fe/H]	Metallicity in dex	0.31 <sup>+0.11</sup> <sub>-0.12</sub>	This work
log( $g$ )	Surface gravity in cgs units	4.669 <sup>+0.025</sup> <sub>-0.022</sub>	This work
$M_*$	Mass in $M_\odot$	0.627 <sup>+0.026</sup> <sub>-0.028</sub>	This work
$R_*$	Radius in $R_\odot$	0.607 <sup>+0.019</sup> <sub>-0.023</sub>	This work
$\rho_*$	Density in g cm <sup>-3</sup>	3.95 <sup>+0.37</sup> <sub>-0.29</sub>	This work
Age	Age in Gyr	7.4 <sup>+4.4</sup> <sub>-4.6</sub>	This work
$A_v$	Visual extinction in mag	0.010 ± 0.007	This work
<b>Other Stellar Parameters</b>			
$v \sin i_*$	Rotational velocity in km s <sup>-1</sup>	<2	This work
RV	RV in km s <sup>-1</sup>	-28.95 ± 0.07	This work

### Notes.

<sup>a</sup> Derived using our modified SpecMatch-Emp algorithm.

<sup>b</sup> EXOFASTv2 derived values using MIST isochrones with the Gaia parallax and spectroscopic parameters in  $a$  as priors.

**References.** Stassun (Stassun et al. 2018), 2MASS (Cutri et al. 2003), Gaia (Gaia Collaboration et al. 2018), SPOC (Jenkins et al. 2016), Bailer-Jones (Bailer-Jones et al. 2018), Green (Green et al. 2019), LAMOST (Zhong et al. 2019), APASS (Henden et al. 2015), WISE (Wright et al. 2010).

Table 3 provides a summary of the inferred system parameters and respective confidence intervals. The uncertainties from the model-dependent stellar parameters are analytically propagated when calculating the values of the parameters  $M_p$ ,  $R_p$ ,  $\rho_p$ ,  $T_{\text{eq}}$ ,  $\langle F \rangle$ , and  $a$ . The data reveal a companion having a mass of  $0.66 \pm 0.07 M_J$  and a radius of  $1.15^{+0.04}_{-0.05} R_J$  transiting TOI-1899 on a  $29.02^{+0.35}_{-0.23}$  day orbit. The majority of the uncertainty (>50% of the  $1\sigma$  confidence intervals) in the mass and radius measurements is due to the quality of the existing observations such that these measurements can be improved with photometry and RVs from more precise instruments.

Given the sparsity of the HPF data, we looked at the generalized Lomb–Scargle (GLS) periodogram (Zechmeister & Kürster 2009) of the RVs to determine if this period solution

was unique. The GLS periodogram is shown in Figure 3(b) with our best-fit period denoted by a vertical line. The RV data only show the existence of orbits near this period, as no other peaks are above a false-alarm probability (FAP) of 0.1%. Panels (c) and (d) of Figure 3 present the result of our joint fit to the photometry and velocimetry.

## 6. Discussion

### 6.1. Stellar Density Diagnostic

We used the stellar density obtained from fitting the SED as a confirmation that the transit occurs on the M dwarf TOI-1899 and not the giant TIC 172370652. The density diagnostic, in which the density derived from a transit is compared to a separate density estimate derived from stellar models, was first



**Table 3**  
Derived Parameters for the TOI-1899 System

Parameter	Units	Value
Photometric Parameters		
Linear limb-darkening coefficient	$u_1$	$0.14^{+0.17}_{-0.10}$
Quadratic limb-darkening coefficient	$u_2$	$0.22^{+0.35}_{-0.23}$
Orbital Parameters		
Orbital period	$P$ (days)	$29.02^{+0.36}_{-0.23}$
Time of periastron	$T_p$ (BJD <sub>TDB</sub> )	$2458,705.37^{+2.28}_{-2.48}$
Eccentricity	$e$	$0.118^{+0.073}_{-0.077}$
Argument of periastron	$\omega$ (deg)	$-13^{+27}_{-28}$
Semi-amplitude velocity	$K$ (m s <sup>-1</sup> )	$59.91^{+6.41}_{-6.32}$
HPF RV offset	$\gamma_{\text{HPF}}$ (m s <sup>-1</sup> )	$16.64^{+5.39}_{-3.23}$
RV jitter	$\sigma_{\text{HPF}}$ (m s <sup>-1</sup> )	$0.39^{+3.84}_{-0.36}$
Transit Parameters		
Time of conjunction	$T_C$ (BJD <sub>TDB</sub> )	$2458,711.957,792^{+0.001182}_{-0.001179}$
Scaled radius	$R_p/R_*$	$0.194^{+0.004}_{-0.005}$
Scaled semimajor axis	$a/R_*$	$56.22^{+1.59}_{-1.66}$
Orbital inclination	$i$ (deg)	$89.77^{+0.15}_{-0.14}$
Impact parameter	$b$	$0.22^{+0.15}_{-0.14}$
Transit duration	$T_{14}$ (hr)	$4.67^{+0.12}_{-0.10}$
Photometric jitter	$\sigma_{\text{TESS}}$ (ppm)	$0.01^{+5.62}_{-0.01}$
Planetary Parameters		
Mass	$M_p$ ( $M_J$ )	$0.66 \pm 0.07$
Radius	$R_p$ ( $R_J$ )	$1.15^{+0.04}_{-0.05}$
Density	$\rho_p$ (g cm <sup>-3</sup> )	$0.54^{+0.09}_{-0.10}$
Surface gravity	$\log(g_p)$ (cgs)	$3.095^{+0.053}_{-0.056}$
Semimajor axis	$a$ (au)	$0.1587^{+0.0067}_{-0.0075}$
Average incident flux	$\langle F \rangle$ (erg s <sup>-1</sup> cm <sup>-2</sup> )	$0.039 \pm 0.003$
Equilibrium temperature <sup>a</sup>	$T_{\text{eq}}$ (K)	$362 \pm 7$

**Note.**

<sup>a</sup> The planet is assumed to be a blackbody.

described by Seager & Mallén-Ornelas (2003) and has been used to examine the planetary nature of candidate planets from Kepler and CoRoT (e.g., Tingley et al. 2011). Gaia DR2 provides a robust constraint on the density of a host star given the parallax and observed photometric magnitudes.

The joint fit includes a prior on the stellar density. As an additional test, we separately fit the TESS photometry and HPF RVs with no density prior. The stellar density derived from the transit with no prior is  $\rho_{*,\text{transit}} = 3.05^{+1.35}_{-1.32}$  g cm<sup>-3</sup>, while the model-dependent density listed in Table 2 is  $\rho_{*,\text{MIST}} = 3.97^{+0.37}_{-0.30}$  g cm<sup>-3</sup>. These values agree to within  $1\sigma$  and are very different from the density of TIC 172370652,  $\rho_* = 0.017^{+0.005}_{-0.004}$  g cm<sup>-3</sup>.

### 6.2. Implications for Planetary Formation

The WJ TOI-1899.01 is the first transiting WJ orbiting an M dwarf and only the fifth M dwarf system with a transiting Jupiter-sized planet (see Figure 4). Studies from RV surveys have shown that most low-eccentricity WJs lack giant planet companions with periods less than a few hundred days (Dong et al. 2014; Bryan et al. 2016) and that metal-poor stars preferentially host low-eccentricity WJs; in contrast, metal-rich star WJs have a range of eccentricities (Dawson & Murray-Clay 2013). An analysis of the Kepler mission (Huang et al.

2016) revealed that Kepler hot Jupiters rarely have detectable inner or outer planetary companions, while half of the Kepler WJs have close, small planetary companions. Huang et al. (2016) postulated that WJs with close planetary companions should have low orbital eccentricities and mutual inclinations, perhaps forming in situ, as theories where WJs form at larger distances and migrate inward (e.g., high-eccentricity tidal migration) result in the scattering of these observed companions. The existence of different populations and formation channels of WJs may be required to fully account for the properties we observe in low- and high-eccentricity WJ systems (Dawson & Johnson 2018).

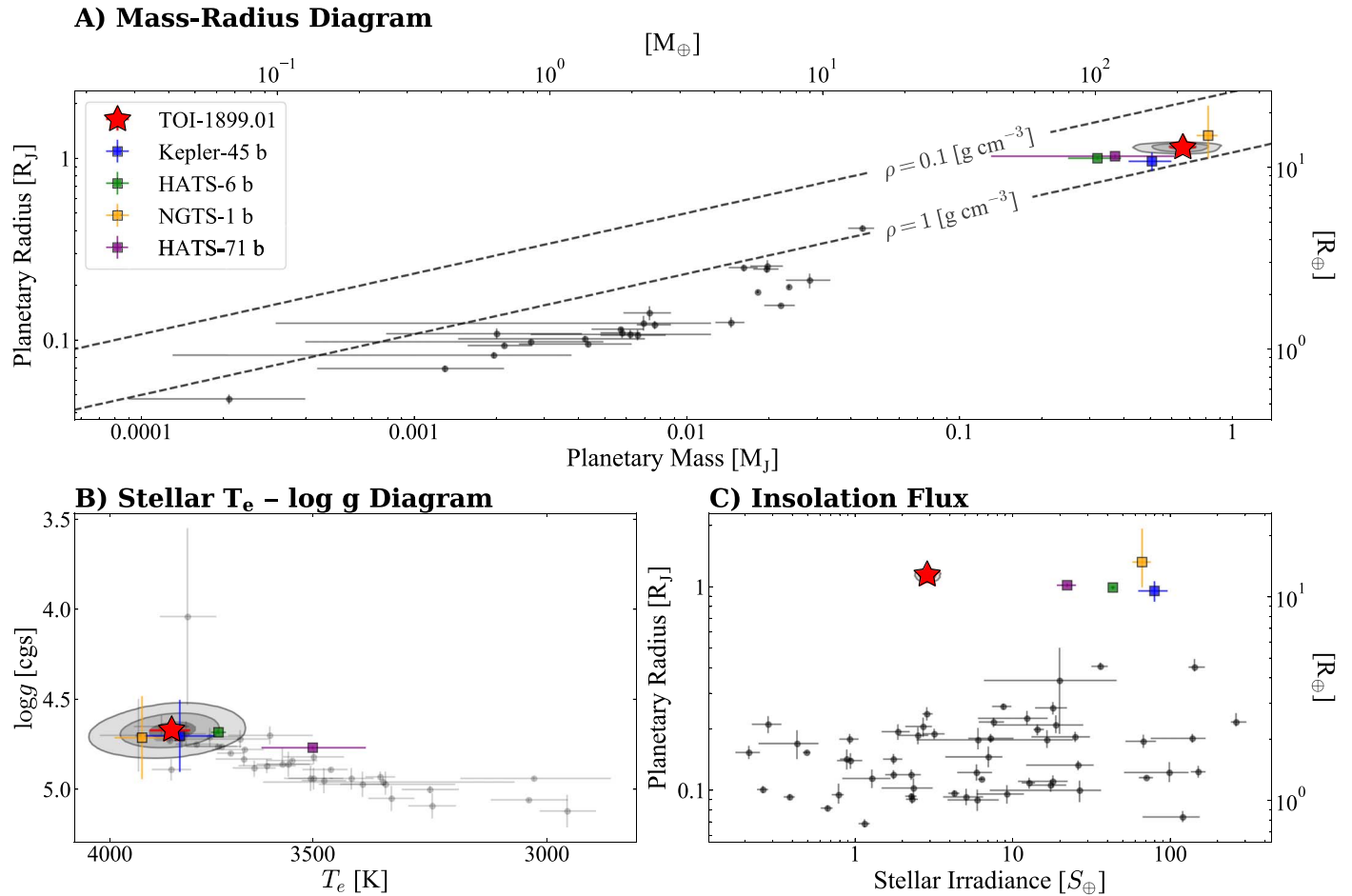
The object TOI-1899.01 is a low-eccentricity ( $e = 0.114^{+0.074}_{-0.076}$ ) WJ orbiting a metal-rich star that the current data suggest lacks close massive planetary companions. It was observed by TESS for a total baseline of 49.9 days. The transit occurs in the middle of this window, and no additional transits or occultations were detected within the data. Our HPF RVs span a total of 56.9 days, and, to determine if the HPF data favored a long-term trend, we jointly modeled the data and included a linear trend. The resulting slope was  $\dot{\gamma} = 0.001 \pm 0.013$  (mm s<sup>-1</sup>) day<sup>-1</sup>, a value well below the sensitivity of HPF that provides evidence that a model with no trend is favored. The lack of additional eclipses and distortions to the standard Keplerian RV curve reveals the lack of an interior ( $P < 29$  days) massive planetary companion. However, TOI-1899 could have additional exoplanets that remain undetected due to their low mass, high inclination, or long orbital periods. Additional photometric and spectroscopic observations are required to further constrain the existence of additional planetary companions.

The measurement of the apparent obliquity through the Rossiter–McLaughlin (RM) effect (Triaud 2018) could provide insight as to how this system formed. A direct measurement of the alignment with the host star via the RM effect would limit the physical processes involved during formation, as some mechanisms, such as disk migration, prohibit high obliquity and misalignment. The TESS photometry shows no activity-induced photometric variability, and a direct measurement of the stellar  $v \sin i_*$  is formally below the resolution of our HPF spectra.

The large depth of this transit could make a direct measurement of the RM effect feasible. As a first-order estimate, if we assume the stellar rotation period is  $\sim 30$  days for a well-aligned star ( $\sin i_* = 1$ ), then  $v \sin i_* = 1$  km s<sup>-1</sup>, and the expected RM effect amplitude is on the order of  $\sim 35$  m s<sup>-1</sup>. While this requires a refined ephemeris, it is within the sensitivity of current precision instruments. The host star is an early M dwarf, and, given the distribution of flux and information content (Reiners et al. 2018), it is not as well suited to observation with an NIR instrument when compared to an optical or red-optical instrument. A high-precision optical instrument, such as HARPS-N (Cosentino et al. 2012), HIRES (Vogt et al. 1994), or CARMENES (Quirrenbach et al. 2014, 2018), would be ideal for a direct RM effect measurement.

### 6.3. Implication for Planetary Interiors and Atmospheres

The WJ TOI-1899 has a large radius when compared to other well-characterized transiting WJs of similar mass (see Figure 5). We compare the observed WJ radii to the radius predicted from models by Baraffe et al. (2008) of a gas giant



**Figure 4.** Physical parameters of the M dwarf TOI-1899 and its WJ. Panel (a) places the WJ, TOI-1899.01, on the mass–radius diagram for all characterized M dwarf exoplanets. For comparison, known hot Jupiters are labeled. Panel (b) highlights the position of TOI-1899 along with other M dwarf–hosting hot Jupiters on a effective temperature–surface gravity diagram. In each of panels (a) and (b), the posterior distribution for the relevant body of TOI-1899 is shown. Panel (c) presents the stellar temperature for the M dwarf exoplanets. Hot Jupiters around M dwarfs are highlighted for comparison. In each panel, the  $1\sigma$ ,  $2\sigma$ , and  $3\sigma$  contours for the posterior distribution are shown for reference. The data were compiled from the NASA Exoplanet Archive (<https://exoplanetarchive.ipac.caltech.edu/cgi-bin/TblView/nph-tblView?app=ExoTbls&config=planets>) on 2020 July 10.

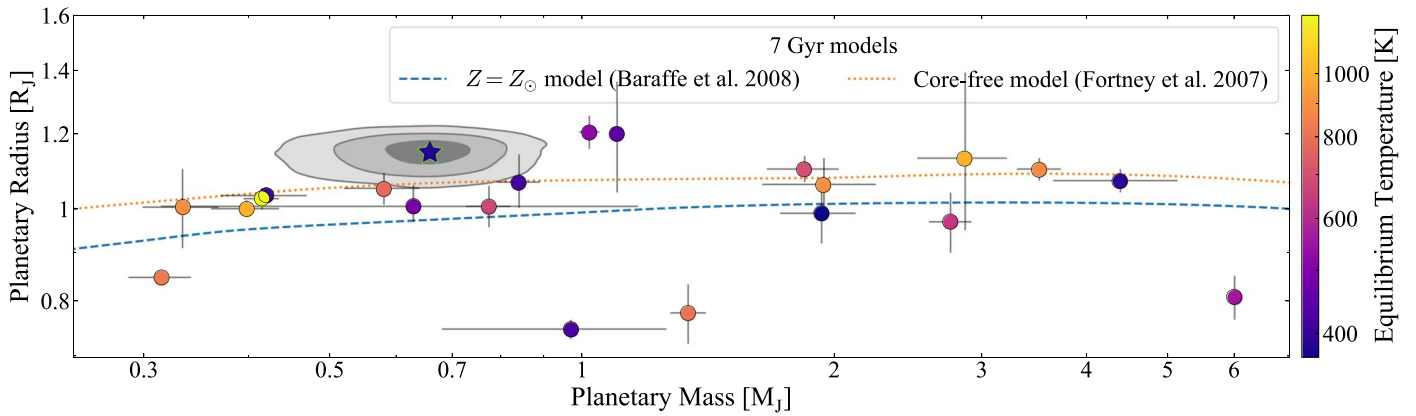
with a solar mixture of H, He, and heavy elements. These models are for nonirradiated planets at varying ages. The observed WJs typically have radii that are within  $1\sigma$  of the predicted values, with the exception of TOI-1899 and Kepler-87 b (Ofir et al. 2014), both of which deviate by  $>3\sigma$  from tracks of comparable ages ( $>1$  Gyr). The radius of TOI-1899.01 may be the result of a very solid-poor composition. As an extreme case, we compare core-free models from Fortney et al. (2007) and find that the planet’s radius is consistent within  $3\sigma$  of that model.

Alternatively, the planet could have an inflated radius; however, stellar flux–driven mechanisms are unlikely to be the cause. Demory & Seager (2011) used a sample of giants in Kepler to determine that gas giants receiving an incident flux  $\lesssim 2 \times 10^8 \text{ erg s}^{-1} \text{ cm}^{-2}$  have radii that are independent of the stellar incident flux. This threshold flux roughly corresponds to an equilibrium temperature for which ohmic heating (Batygin et al. 2011) is thought to become important in heating the inner layers of a gas giant. The WJ TOI-1899.01 receives an average flux of  $0.039 \times 10^8 \text{ erg s}^{-1} \text{ cm}^{-2}$ , a value well below this limit.

One possible mechanism that could result in the inflated radius despite the low stellar irradiation is delayed contraction. Baraffe et al. (2014) described two variations of delayed contraction due to an enhancement in atmospheric opacities

(Burrows et al. 2007) or a reduction in the interior heat transport of a planet (Chabrier & Baraffe 2007). Burrows et al. (2007) suggested that an atmosphere with enhanced opacities (e.g., through enhanced atmospheric metallicity) would slow the cooling of a planet and maintain a larger radius for longer periods of time. This may not be an effective method of inflation, as a larger opacity through enrichment of the atmosphere requires an increased molecular weight, which may result in a smaller radius in the absence of extensive stellar irradiation (e.g., Guillot 2005, 2008). The second variation of delayed contraction was suggested by Chabrier & Baraffe (2007), where the presence of a gradient of heavy elements can decrease the heat transport efficiency and slow down planetary cooling and contraction. A gradient in the mean molecular weight can prevent large-scale convection, disrupting heat transport and resulting in a semiconvective layer independent of stellar incident flux. Additional photometric observations of TOI-1899.01 are required to identify its atmospheric properties and composition and determine if the atmosphere is enriched or if nonobservable chemical gradients must be considered to inflate the radius of TOI-1899.01.

The large radius suggests that TOI-1899.01 has a large atmospheric scale height and, potentially, large transmission spectral signals. It is cool enough that we expect the presence



**Figure 5.** TOI-1899.01 compared to transiting WJs. This panel presents the mass–radius diagram for transiting WJs. The  $1\sigma$ ,  $2\sigma$ , and  $3\sigma$  posteriors for TOI-1899 from our fit are included for reference. We include models from Baraffe et al. (2008) for Jovian planets at various ages without the effects of stellar irradiation. Here TOI-1899.01 is slightly larger than WJs of comparable mass and deviates by  $>3\sigma$  from the model from Baraffe et al. (2008) for a 7 Gyr system. The radius is consistent within  $3\sigma$  with a core-free model of a 7 Gyr system from Fortney et al. (2007) such that the large radius may result from a low solid content. It is one of the largest WJs, and, given one of the lowest equilibrium temperatures, the mechanism for this inflation cannot be stellar flux-driven. The data were compiled from the NASA Exoplanet Archive (<https://exoplanetarchive.ipac.caltech.edu/cgi-bin/TblView/nph-tblView?app=ExoTbls&config=planets>) on 2020 July 10.

of molecular clouds (e.g., Burrows & Sharp 1999; Morley et al. 2014). Sing et al. (2016) demonstrated that while it is possible to detect the absorption feature of various molecular species in gas giants, it is difficult to predict the spectral features of a particular exoplanet given the wide range in surface gravity, metallicity, and temperatures for these objects. All of these parameters can affect a planet’s atmospheric structure, circulation, and condensate formation, which in turn impact the observable features. If we assume that the composition of the atmosphere is dominated by a hydrogen–helium mixture (Sing 2018) and ignore the presence of clouds, we estimate absorption features with amplitudes on the order of 150 ppm. From existing atmospheric models for giant planets, we expect that the presence and height of condensates would weaken or even erase spectral features (e.g., Marley et al. 1999; Sudarsky et al. 2003; Fortney 2005; Morley et al. 2014). The presence of clouds has served as a possible explanation for the weak water features of HD 209458 b (Deming et al. 2013) and HAT-P-12 b (Line et al. 2013) and the featureless spectra of GJ 1214 b (Kreidberg et al. 2014) and GJ 436 b (Knutson et al. 2014). In the infrared, the scattering and absorption efficiencies of condensates change and can produce windows where the spectra are not significantly affected by certain clouds (Morley et al. 2014). Upcoming missions, such as the James Webb Space Telescope (JWST), will have the precision and wavelength coverage to attempt these measurements. The JWST transmission spectra of a cloudy atmosphere have the potential to constrain key model atmospheric parameters such as metallicity, C/O ratio, and various cloud parameters for cool WJs (Mai & Line 2019).

## 7. Summary

We have confirmed the planetary nature of an object creating a single transit in a star observed by TESS. The object TOI-1899.01 is the first WJ transiting an M dwarf in a low-eccentricity  $\sim 29$  day orbit. The available data do not provide evidence for massive interior planetary companions. In the population of well-characterized WJs, this planet stands out as an inflated, cool object. It is among the largest in radii, which may point toward a low fraction in solids or possibly inflation despite its cool temperature. The long period of TOI-1899.01

has the potential to make ground-based transit searches difficult, but it should be amenable to additional observations with space assets, such as the recently launched CHaracterizing ExOPlanet Satellite mission (CHEOPS; Broeg et al. 2013; Fortier et al. 2014). CHEOPS has the potential to detect an additional transit for a significant fraction ( $\sim 70\%$ ; Cooke et al. 2020) of single-transiting objects, such as TOI-1899, that were observed during the primary TESS mission. Future observations that can provide information on the atmospheric properties or formation pathways, such as atmospheric characterization or a stellar obliquity measurement, are dependent on a more precise ephemeris. We urge the community to observe this system with additional RV observations as well as for additional transits to precisely determine the period and refine constraints on the eccentricity.

We thank the anonymous referee for a thoughtful reading of the manuscript and comments that improved the quality of this publication. C.I.C. and G.K.S. acknowledge support by NASA Headquarters under the NASA Earth and Space Science Fellowship Program through grants 80NSSC18K1114 and NNX16AO28H, respectively. C.I.C. acknowledges support by the Alfred P. Sloan Foundation’s Minority Ph.D. Program under grant G-2016-20166039. G.K.S. is also supported by the Henry Norris Russell Fellowship at Princeton University. H.M.L. acknowledges support from NSF grant AST 1616636. R.I.D. acknowledges support from grant NNX16AB50G awarded by the NASA Exoplanets Research Program and the Alfred P. Sloan Foundation’s Sloan Research Fellowship.

This work was partially supported by funding from the Center for Exoplanets and Habitable Worlds (CEHW). CEHW is supported by the Pennsylvania State University, the Eberly College of Science, and the Pennsylvania Space Grant Consortium.

This is University of Texas Center for Planetary Systems Habitability Contribution 0004. These results are based on observations obtained with the Habitable-zone Planet Finder Spectrograph on the HET. We acknowledge support from NSF grants AST 1006676, AST 1126413, AST 1310875, and AST 1310885 and the NASA Astrobiology Institute (NNA09-DA76A) in our pursuit of precision radial velocities in the NIR. We acknowledge support from the Heising-Simons

Foundation via grant 2017-0494. The Hobby–Eberly Telescope is a joint project of the University of Texas at Austin, the Pennsylvania State University, Ludwig-Maximilians-Universität München, and Georg-August Universität Göttingen. The HET is named in honor of its principal benefactors, William P. Hobby and Robert E. Eberly. The HET collaboration acknowledges the support and resources from the Texas Advanced Computing Center. We thank the resident astronomers and telescope operators at the HET for the skillful execution of our observations with HPF.

We acknowledge support from NSF grant AST-1909506 and the Research Corporation for precision photometric observations with diffuser-assisted photometry.

Part of this research was carried out at the Jet Propulsion Laboratory, California Institute of Technology, under a contract with the National Aeronautics and Space Administration (NASA).

Computations for this research were performed on the Pennsylvania State University’s Institute for Computational and Data Sciences Advanced CyberInfrastructure (ICDS-ACI), including the CyberLAMP cluster supported by NSF grant MRI-1626251.

These results are based on observations obtained with the 3 m Shane Telescope at Lick Observatory. The authors thank the Shane Telescope operators, AO operators, and laser operators for their assistance in obtaining these data.

Some of the observations in this paper made use of the NN-EXPLORE Exoplanet and Stellar Speckle Imager (NESSI). NESSI was funded by the NASA Exoplanet Exploration Program and the NASA Ames Research Center. NESSI was built at the Ames Research Center by Steve B. Howell, Nic Scott, Elliott P. Horch, and Emmett Quigley.

These results are based on observations obtained with Apache Point Observatory’s 0.5 m ARCSAT.

Some of the data presented in this paper were obtained from MAST. Support for MAST for non-HST data is provided by the NASA Office of Space Science via grant NNX09AF08G and by other grants and contracts. This work includes data collected by the TESS mission that are publicly available from MAST. Funding for the TESS mission is provided by the NASA Science Mission Directorate. This research made use of the NASA Exoplanet Archive, which is operated by Caltech, under contract with NASA under the Exoplanet Exploration Program. This work includes data from 2MASS, which is a joint project of the University of Massachusetts and IPAC at Caltech funded by NASA and the NSF.

We acknowledge with thanks the variable star observations from the AAVSO International Database contributed by observers worldwide and used in this research.

This work has made use of data from the European Space Agency (ESA) mission Gaia (<https://www.cosmos.esa.int/gaia>), processed by the Gaia Data Processing and Analysis Consortium (DPAC; <https://www.cosmos.esa.int/web/gaia/dpac/consortium>). Funding for the DPAC has been provided by national institutions, in particular the institutions participating in the Gaia Multilateral Agreement.

Some observations were obtained with the Samuel Oschin 48 inch Telescope at the Palomar Observatory as part of the ZTF project. The ZTF is supported by the NSF under grant No. AST-1440341 and a collaboration including Caltech, IPAC, the Weizmann Institute for Science, the Oskar Klein Center at Stockholm University, the University of Maryland, the






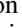

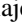



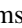

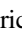
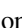

University of Washington, Deutsches Elektronen-Synchrotron and Humboldt University, Los Alamos National Laboratories, the TANGO Consortium of Taiwan, the University of Wisconsin at Milwaukee, and Lawrence Berkeley National Laboratories. Operations are conducted by COO, IPAC, and UW.




This work has made use of data from the Guoshoujing Telescope (LAMOST), a National Major Scientific Project built by the Chinese Academy of Sciences. Funding for the project has been provided by the National Development and Reform Commission. LAMOST is operated and managed by the National Astronomical Observatories, Chinese Academy of Sciences.

*Facilities:* AAVSO, Gaia, HET (HPF), KPNO (HDI), LAMOST, PO:1.2 m (ZTF), Shane (AO), TESS, WIYN (NESSI).

*Software:* AstroImageJ (Collins et al. 2017), astroquery (Ginsburg et al. 2019), astropy (Astropy Collaboration et al. 2018), barycorrpy (Kanodia & Wright 2018), batman (Kreidberg 2015), celerite (Foreman-Mackey et al. 2017), ccdproc (Craig et al. 2017), dustmaps (Green 2018), DAVE (Kostov et al. 2019), EXOFASTv2 (Eastman et al. 2019), HxRGproc (Ninan et al. 2018), GNU Parallel (Tange 2011), juliet (Espinoza et al. 2019), lightkurve (Lightkurve Collaboration et al. 2018), matplotlib (Hunter 2007), MultiNest (Feroz et al. 2009, 2019), numpy (van der Walt et al. 2011), pandas (McKinney 2010), Photutils (Bradley et al. 2019), radvel (Fulton et al. 2018), scipy (Virtanen et al. 2020), SERVAL, SpecMatch-Emp, VESPA (Morton 2012).

## ORCID iDs

Caleb I. Cañas  <https://orcid.org/0000-0003-4835-0619>  
 Gudmundur Stefansson  <https://orcid.org/0000-0001-7409-5688>  
 Shubham Kanodia  <https://orcid.org/0000-0001-8401-4300>  
 Suvrath Mahadevan  <https://orcid.org/0000-0001-9596-7983>  
 William D. Cochran  <https://orcid.org/0000-0001-9662-3496>  
 Michael Endl  <https://orcid.org/0000-0002-7714-6310>  
 Paul Robertson  <https://orcid.org/0000-0003-0149-9678>  
 Chad F. Bender  <https://orcid.org/0000-0003-4384-7220>  
 Joe P. Ninan  <https://orcid.org/0000-0001-8720-5612>  
 Corey Beard  <https://orcid.org/0000-0001-7708-2364>  
 Jack Lubin  <https://orcid.org/0000-0001-8342-7736>  
 Arvind F. Gupta  <https://orcid.org/0000-0002-5463-9980>  
 Mark E. Everett  <https://orcid.org/0000-0002-0885-7215>  
 Andrew Monson  <https://orcid.org/0000-0002-0048-2586>  
 Robert F. Wilson  <https://orcid.org/0000-0002-4235-6369>  
 Hannah M. Lewis  <https://orcid.org/0000-0002-7871-085X>  
 Steven R. Majewski  <https://orcid.org/0000-0003-2025-3147>  
 Leslie Hebb  <https://orcid.org/0000-0003-1263-8637>  
 Rebekah I. Dawson  <https://orcid.org/0000-0001-9677-1296>  
 Scott A. Diddams  <https://orcid.org/0000-0002-2144-0764>  
 Eric B. Ford  <https://orcid.org/0000-0001-6545-639X>  
 Connor Fredrick  <https://orcid.org/0000-0002-0560-1433>  
 Samuel Halverson  <https://orcid.org/0000-0003-1312-9391>  
 Fred Hearty  <https://orcid.org/0000-0002-1664-3102>  
 Andrea S. J. Lin  <https://orcid.org/0000-0002-9082-6337>  
 Andrew J. Metcalf  <https://orcid.org/0000-0001-5000-1018>

Jayadev Rajagopal  <https://orcid.org/0000-0002-2488-7123>  
 Arpita Roy  <https://orcid.org/0000-0001-8127-5775>  
 Christian Schwab  <https://orcid.org/0000-0002-0091-7105>  
 Ryan C. Terrien  <https://orcid.org/0000-0002-4788-8858>  
 Jason T. Wright  <https://orcid.org/0000-0001-6160-5888>

## References

- Albrecht, S., Winn, J. N., Johnson, J. A., et al. 2012, *ApJ*, **757**, 18  
 Anglada-Escudé, G., & Butler, R. P. 2012, *ApJS*, **200**, 15  
 Astropy Collaboration, Price-Whelan, A. M., Sipőcz, B. M., et al. 2018, *AJ*, **156**, 123  
 Bailer-Jones, C. A. L., Rybizki, J., Foesneau, M., Mantelet, G., & Andrae, R. 2018, *AJ*, **156**, 58  
 Baraffe, I., Chabrier, G., & Barman, T. 2008, *A&A*, **482**, 315  
 Baraffe, I., Chabrier, G., Fortney, J., & Sotin, C. 2014, in *Protostars and Planets VI*, ed. H. Beuther et al. (Tucson, AZ: Univ. Arizona Press), 763  
 Batygin, K., Stevenson, D. J., & Bodenheimer, P. H. 2011, *ApJ*, **738**, 1  
 Bakos, G. Á., Bayliss, D., Bento, J., et al. 2020, *AJ*, **159**, 267  
 Bayliss, D., Gillen, E., Eigmüller, P., et al. 2018, *MNRAS*, **475**, 4467  
 Bonfils, X., Delfosse, X., Udry, S., et al. 2013, *A&A*, **549**, A109  
 Bradley, L., Sipőcz, B., Robitaille, T., et al. 2019, *astropy/photutils*: v0.6, Zenodo, doi:10.5281/zenodo.2533376  
 Broeg, C., Fortier, A., Ehrenreich, D., et al. 2013, *EPJWC*, **47**, 03005  
 Bryan, M. L., Knutson, H. A., Howard, A. W., et al. 2016, *ApJ*, **821**, 89  
 Bryson, S. T., Jenkins, J. M., Gilliland, R. L., et al. 2013, *PASP*, **125**, 889  
 Buchner, J., Georgakakis, A., Nandra, K., et al. 2014, *A&A*, **564**, A125  
 Burrows, A., Hubeny, I., Budaj, J., & Hubbard, W. B. 2007, *ApJ*, **661**, 502  
 Burrows, A., & Sharp, C. M. 1999, *ApJ*, **512**, 843  
 Chabrier, G., & Baraffe, I. 2007, *ApJL*, **661**, L81  
 Choi, J., Dotter, A., Conroy, C., et al. 2016, *ApJ*, **823**, 102  
 Clough, S. A., Shephard, M. W., Mlawer, E. J., et al. 2005, *JQSR*, **91**, 233  
 Collins, K. A., Kielkopf, J. F., Stassun, K. G., & Hessman, F. V. 2017, *AJ*, **153**, 77  
 Cooke, B. F., Pollacco, D., Lendl, M., Kuntzer, T., & Fortier, A. 2020, *MNRAS*, **494**, 736  
 Cosentino, R., Lovis, C., Pepe, F., et al. 2012, *Proc. SPIE*, **8446**, 84461V  
 Craig, M., Crawford, S., Seifert, M., et al. 2017, *astropy/ccdproc*: v1.3.0.post1, Zenodo, doi:10.5281/zenodo.1069648  
 Cui, X.-Q., Zhao, Y.-H., Chu, Y.-Q., et al. 2012, *RAA*, **12**, 1197  
 Cutri, R. M., Skrutskie, M. F., van Dyk, S., et al. 2003, *yCat*, **2246**, 0  
 Dawson, R. I., & Johnson, J. A. 2018, *ARA&A*, **56**, 175  
 Dawson, R. I., & Murray-Clay, R. A. 2013, *ApJL*, **767**, L24  
 Delfosse, X., Forveille, T., Mayor, M., et al. 1998, *A&A*, **338**, L67  
 Deliyannis, C. P. 2013, AAS Meeting, **222**, 111.06  
 Deming, D., Wilkins, A., McCullough, P., et al. 2013, *ApJ*, **774**, 95  
 Demory, B.-O., & Seager, S. 2011, *ApJS*, **197**, 12  
 Dong, S., Katz, B., & Socrates, A. 2014, *ApJL*, **781**, L5  
 Dotter, A. 2016, *ApJS*, **222**, 8  
 Eastman, J. D., Rodríguez, J. E., Agol, E., et al. 2019, arXiv:1907.09480  
 Eisner, N. L., Barragán, O., Aigrain, S., et al. 2020, *MNRAS*, **494**, 750  
 Endl, M., Cochran, W. D., Kürster, M., et al. 2006, *ApJ*, **649**, 436  
 Espinoza, N., Kossakowski, D., & Brahm, R. 2019, *MNRAS*, **490**, 2262  
 Feinstein, A. D., Montet, B. T., Foreman-Mackey, D., et al. 2019, *PASP*, **131**, 094502  
 Feroz, F., Hobson, M. P., & Bridges, M. 2009, *MNRAS*, **398**, 1601  
 Feroz, F., Hobson, M. P., Cameron, E., & Pettitt, A. N. 2019, *OJAp*, **2**, 10  
 Fitzpatrick, E. L. 1999, *PASP*, **111**, 63  
 Foreman-Mackey, D., Agol, E., Ambikasaran, S., & Angus, R. 2017, *AJ*, **154**, 220  
 Fortier, A., Beck, T., Benz, W., et al. 2014, *Proc. SPIE*, **9143**, 91432J  
 Fortney, J. J. 2005, *MNRAS*, **364**, 649  
 Fortney, J. J., Marley, M. S., & Barnes, J. W. 2007, *ApJ*, **659**, 1661  
 Fulton, B. J., Petigura, E. A., Blunt, S., & Sinukoff, E. 2018, *PASP*, **130**, 044504  
 Furlan, E., Ciardi, D. R., Everett, M. E., et al. 2017, *AJ*, **153**, 71  
 Gaia Collaboration, Brown, A. G. A., Vallenari, A., et al. 2018, *A&A*, **616**, A1  
 Gaidos, E., Mann, A. W., Lépine, S., et al. 2014, *MNRAS*, **443**, 2561  
 Ginsburg, A., Sipőcz, B. M., Brasseur, C. E., et al. 2019, *AJ*, **157**, 98  
 Green, G. M. 2018, *JOSS*, **3**, 695  
 Green, G. M., Schlafly, E., Zucker, C., Speagle, J. S., & Finkbeiner, D. 2019, *ApJ*, **887**, 93  
 Guillot, T. 2005, *AREPS*, **33**, 493  
 Guillot, T. 2008, *PhST*, **130**, 014023  
 Gullikson, K., Dodson-Robinson, S., & Kraus, A. 2014, *AJ*, **148**, 53  
 Hartman, J. D., Bayliss, D., Brahm, R., et al. 2015, *AJ*, **149**, 166  
 Henden, A. A., Levine, S., Terrell, D., & Welch, D. L. 2015, AAS Meeting, **225**, 336.16  
 Hilton, E. J., Hawley, S. L., Kowalski, A. F., & Holtzman, J. 2011, in *ASP Conf. Ser. 448, The Galactic M Dwarf Flare Rate*, ed. C. Johns-Krull, M. K. Browning, & A. A. West (San Francisco, CA: ASP), 197  
 Howell, S. B., Everett, M. E., Sherry, W., Horch, E., & Ciardi, D. R. 2011, *AJ*, **142**, 19  
 Huang, C., Wu, Y., & Triaud, A. H. M. J. 2016, *ApJ*, **825**, 98  
 Hunter, J. D. 2007, *CSE*, **9**, 90  
 Jenkins, J. M., Caldwell, D. A., & Borucki, W. J. 2002, *ApJ*, **564**, 495  
 Jenkins, J. M., Caldwell, D. A., Chandrasekaran, H., et al. 2010, *ApJL*, **713**, L87  
 Jenkins, J. M., Twicken, J. D., McCauliff, S., et al. 2016, *Proc. SPIE*, **9913**, 99133E  
 Johnson, J. A., Aller, K. M., Howard, A. W., & Crepp, J. R. 2010, *PASP*, **122**, 905  
 Johnson, J. A., Gazak, J. Z., Apps, K., et al. 2012, *AJ*, **143**, 111  
 Kanodia, S., & Wright, J. 2018, *RNAAS*, **2**, 4  
 Kipping, D. M., Hartman, J., Buchhave, L. A., et al. 2013, *ApJ*, **770**, 101  
 Knutson, H. A., Benneke, B., Deming, D., & Homeier, D. 2014, *Natur*, **505**, 66  
 Kochanek, C. S., Shappee, B. J., Stanek, K. Z., et al. 2017, *PASP*, **129**, 104502  
 Kostov, V. B., Mullally, S. E., Quintana, E. V., et al. 2019, *AJ*, **157**, 124  
 Kovács, G., Zucker, S., & Mazeh, T. 2002, *A&A*, **391**, 369  
 Kreidberg, L. 2015, *batman*: Basic Transit Model cAlculation in Python, version 2.46, Astrophysics Source Code Library, ascl:1510.002  
 Kreidberg, L., Bean, J. L., Désert, J.-M., et al. 2014, *Natur*, **505**, 69  
 Laughlin, G., Bodenheimer, P., & Adams, F. C. 2004, *ApJL*, **612**, L73  
 Lépine, S., Rich, R. M., & Shara, M. M. 2007, *ApJ*, **669**, 1235  
 Lightkurve Collaboration, Cardoso, J. V. d. M. a., Hedges, C., et al. 2018, *Lightkurve*: Kepler and TESS Time Series Analysis in Python, version 1.11.1, Astrophysics Source Code Library, ascl:1812.013  
 Li, G., & Winn, J. N. 2016, *ApJ*, **818**, 5  
 Line, M. R., Knutson, H., Deming, D., Wilkins, A., & Desert, J.-M. 2013, *ApJ*, **778**, 183  
 Mahadevan, S., Ramsey, L., Bender, C., et al. 2012, *Proc. SPIE*, **8446**, 84461S  
 Mahadevan, S., Ramsey, L. W., Terrien, R., et al. 2014, *Proc. SPIE*, **9147**, 91471G  
 Mai, C., & Line, M. R. 2019, *ApJ*, **883**, 144  
 Mandel, K., & Agol, E. 2002, *ApJL*, **580**, L171  
 Mann, A. W., Brewer, J. M., Gaidos, E., Lépine, S., & Hilton, E. J. 2013, *AJ*, **145**, 52  
 Marcy, G. W., Butler, R. P., Vogt, S. S., Fischer, D., & Lissauer, J. J. 1998, *ApJL*, **505**, L147  
 Marley, M. S., Gelino, C., Stephens, D., Lunine, J. I., & Freedman, R. 1999, *ApJ*, **513**, 879  
 Masi, F. J., Laher, R. R., Rusholme, B., et al. 2019, *PASP*, **131**, 018003  
 McKinney, W. 2010, in *Proc. 9th Python in Science Conf.*, ed. S. van der Walt & J. Millman (Austin, TX: SciPy), 51  
 Metcalf, A., Anderson, T., Bender, C., et al. 2019, *Optic*, **6**, 233  
 Morales, J. C., Mustill, A. J., Ribas, I., et al. 2019, *Sci*, **365**, 1441  
 Morley, C. V., Marley, M. S., Fortney, J. J., et al. 2014, *ApJ*, **787**, 78  
 Morton, T. D. 2012, *ApJ*, **761**, 6  
 Morton, T. D., Bryson, S. T., Coughlin, J. L., et al. 2016, *ApJ*, **822**, 86  
 Ninan, J. P., Bender, C. F., Mahadevan, S., et al. 2018, *Proc. SPIE*, **10709**, 107092U  
 Ofir, A., Dreizler, S., Zechmeister, M., & Husser, T.-O. 2014, *A&A*, **561**, A103  
 Queiroz, A. B. A., Anders, F., Santiago, B. X., et al. 2018, *MNRAS*, **476**, 2556  
 Quirrenbach, A., Amado, P. J., Caballero, J. A., et al. 2014, *Proc. SPIE*, **9147**, 91471F  
 Quirrenbach, A., Amado, P. J., Ribas, I., et al. 2018, *Proc. SPIE*, **10702**, 107020W  
 Reiners, A., Zechmeister, M., Caballero, J. A., et al. 2018, *A&A*, **612**, A49  
 Ricker, G., & Vanderspek, R. 2018, *Data Products From TESS Data Alerts, (TESS-DATA-ALERTS), STScI/MAST*,  
 Santiago, B. X., Brauer, D. E., Anders, F., et al. 2016, *A&A*, **585**, A42  
 Scott, N. J., Howell, S. B., Horch, E. P., & Everett, M. E. 2018, *PASP*, **130**, 054502  
 Seager, S., & Mallén-Ornelas, G. 2003, *ApJ*, **585**, 1038  
 Shetrone, M., Cornell, M. E., Fowler, J. R., et al. 2007, *PASP*, **119**, 556  
 Sing, D. K. 2018, arXiv:1804.07357  
 Sing, D. K., Fortney, J. J., Nikolov, N., et al. 2016, *Natur*, **529**, 59  
 Skrutskie, M. F., Cutri, R. M., Stiening, R., et al. 2006, *AJ*, **131**, 1163  
 Srinath, S., McGurk, R., Rockosi, C., et al. 2014, *Proc. SPIE*, **9148**, 91482Z  
 Stassun, K. G., Oelkers, R. J., Paegert, M., et al. 2019, *AJ*, **158**, 138  
 Stassun, K. G., Oelkers, R. J., Pepper, J., et al. 2018, *AJ*, **156**, 102

- Stefansson, G., Cañas, C., Wisniewski, J., et al. 2020, *AJ*, 159, 100
- Stefansson, G., Hearty, F., Robertson, P., et al. 2016, *ApJ*, 833, 175
- Stefansson, G., Li, Y., Mahadevan, S., et al. 2018, *AJ*, 156, 266
- Stefansson, G., Mahadevan, S., Hebb, L., et al. 2017, *ApJ*, 848, 9
- Sudarsky, D., Burrows, A., & Hubeny, I. 2003, *ApJ*, 588, 1121
- Sullivan, P. W., Winn, J. N., Berta-Thompson, Z. K., et al. 2015, *ApJ*, 809, 77
- Tange, O. 2011, login: The USENIX Magazine, 36, 42, Zenodo, doi:10.5281/zenodo.16303
- Tenenbaum, P., Jenkins, J. M., Seader, S., et al. 2013, *ApJS*, 206, 5
- Tingley, B., Bonomo, A. S., & Deeg, H. J. 2011, *ApJ*, 726, 112
- Triaud, A. H. M. J. 2018, in *Handbook of Exoplanets*, ed. H. Deeg & J. Belmonte (Cham: Springer), 2
- Tucker, D. L., Kent, S., Richmond, M. W., et al. 2006, *AN*, 327, 821
- van der Walt, S., Colbert, S. C., & Varoquaux, G. 2011, *CSE*, 13, 22
- van Roestel, J., Bellm, E. C., Duev, D. A., et al. 2019, *RNAAS*, 3, 136
- Virtanen, P., Gommers, R., Oliphant, T. E., et al. 2020, *NatMe*, 17, 261
- Vogt, S. S., Allen, S. L., Bigelow, B. C., et al. 1994, *Proc. SPIE*, 2198, 362
- Wright, E. L., Eisenhardt, P. R. M., Mainzer, A. K., et al. 2010, *AJ*, 140, 1868
- Wright, J. T., & Eastman, J. D. 2014, *PASP*, 126, 838
- Yee, S. W., Petigura, E. A., & von Braun, K. 2017, *ApJ*, 836, 77
- York, D. G., Adelman, J., Anderson, J. E. J., et al. 2000, *AJ*, 120, 1579
- Zechmeister, M., & Kürster, M. 2009, *A&A*, 496, 577
- Zechmeister, M., Reiners, A., Amado, P. J., et al. 2018, *A&A*, 609, A12
- Zhong, J., Li, J., Carlin, J. L., et al. 2019, *ApJS*, 244, 8
- Zong, W., Fu, J.-N., De Cat, P., et al. 2018, *ApJS*, 238, 30